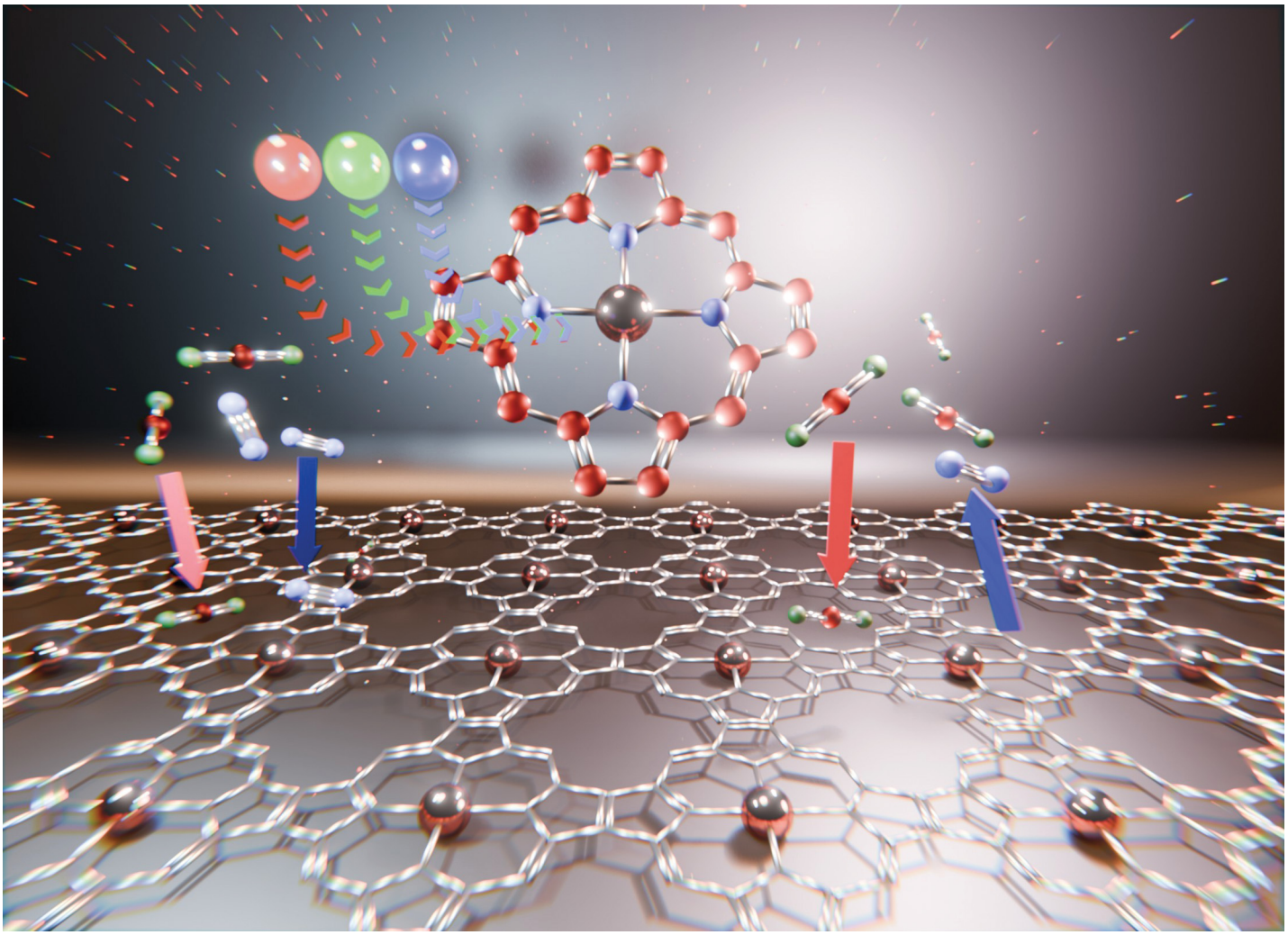

Showcasing research from Dr Mandeep Chahal's laboratory, Chemistry and Forensic Science, School of Natural Sciences, University of Kent, Canterbury, United Kingdom.

Central-metal-cation-based modulation of gas adsorption selectivity in porous tetrapyrrolic materials

This work introduces a viable strategy for developing porous CO_2 adsorbent materials using tetrapyrrolic building blocks by avoiding complex bottom-up synthesis. The resulting materials demonstrate enhanced CO_2 adsorption performance, highlighting their potential for carbon capture applications.

Image reproduced by permission of Mandeep K. Chahal from *Chem. Commun.*, 2026, **62**, 5227.

As featured in:

See Mandeep K. Chahal *et al.*, *Chem. Commun.*, 2026, **62**, 5227.

ROYAL SOCIETY OF CHEMISTRY

rsc.li/chemcomm

Registered charity number: 207890

ChemComm

COMMUNICATION

View Article Online
View Journal | View Issue

Cite this: *Chem. Commun.*, 2026, **62**, 5227

Received 29th November 2025,
Accepted 9th February 2026

DOI: 10.1039/d5cc06796k

rsc.li/chemcomm

Central-metal-cation-based modulation of gas adsorption selectivity in porous tetrapyrrolic materials

Subrata Maji,[a] Prachi Gupta,[b] Rob Clowes,[b] Yoshitaka Matsushita,[c] Lok Kumar Shrestha,[a] Anna G. Slater,[b] Jonathan P. Hill[a] and Mandeep K. Chahal*[d]

We present a direct strategy to assemble porous tetrapyrrolic materials with tunable gas uptake selectivity by varying the coordinated cation. Co-OX1 shows improved CO_2 uptake of 51.66 cm^3 g^{-1} at 298 K, while free base-OX1 demonstrates a CO_2/N_2 selectivity of 202.9. This approach offers a viable route to CO_2 capture technologies.

A critical driver of climate change is the rising level of atmospheric CO_2, which threatens human health, ecosystems, food security and the global economy.[1,2] Porous materials are suitable candidates for applications in gas capture technologies.[3–5] Known porous solids such as zeolites, metal–organic frameworks (MOFs), and covalent organic frameworks (COFs), offer high gas adsorption capacity and selectivity but suffer from poor processability.[6–8] However, once formed, these porous network materials are difficult to disperse in most media, making deposition on substrates challenging and obstructing applications. As an alternative, porous organic molecular materials such as hydrogen- and halogen-bonded organic frameworks (HOF, XOF, resp.), porous organic cages, supramolecular organic frameworks (SOFs), and π-organic frameworks, lack strong intermolecular bonds between building blocks[9–12] enabling processing from solution as porous solids or liquids. These porous materials offer various advantages such as ease of structural characterisation, solution processability, tunability, modularity, and ease of regeneration.

Since the emergence of the processable porous materials field, porphyrin-based cages, HOFs, and SOFs have been reported based on intrinsic and/or extrinsic porous networks.[13–18] Porphyrins are particularly attractive components of porous materials due to their unique tunable photophysical, photochemical, and electrochemical properties, which allow adaptation to specific functional roles. Topological and pore structure modulation without a requirement for *de novo* design is crucial in porous materials, enabling precise control over molecular diffusion, adsorption selectivity, and host–guest interactions.[19,20] For porphyrinic HOFs, pore engineering has recently been achieved by introducing structure-directing agents (SDAs) such as solvents,[16,21] or small cations[22] or by varying metal cation coordination.[23–25]

In general, the metal cation in metalloporphyrins controls the macrocyclic geometry, axial coordination, electronic structure, and intermolecular interactions. Although variation of the coordinated metal cation is known to affect textural properties in metalloporphyrin-based HOFs,[23–25] there are no reports so far showing that metalation of porphyrins can influence the selectivity of gas adsorption. Despite this, metalation remains a powerful strategy to generate novel porous materials from existing porphyrin building blocks. This raises the intriguing possibility that metalation might be used as a design tool not only to enhance structural stability and engineer pore structure, but also to enable effective access to new processable porous materials with selective gas storage and sensing capabilities.

We have recently reported a nickel-porphyrin-based porous processable framework material that enables highly sensitive

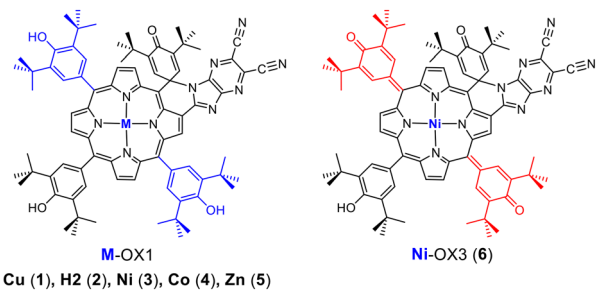

Fig. 1 Chemical structures of M-OX1 and Ni-OX3 compounds synthesised to investigate the effect of metal cations on porous framework structure and gas adsorption selectivity.

[a] *Research Center for Materials Nanoarchitectonics, National Institute for Materials Science, 1-1 Namiki, Tsukuba, Ibaraki 305-0044, Japan*
[b] *Department of Chemistry and Materials Innovation Factory, University of Liverpool, Liverpool L69 7ZD, UK*
[c] *Research Network and Facility Services Division, National Institute for Materials Science, 1-2-1 Sengen, Tsukuba, Ibaraki 305-0047, Japan*
[d] *Chemistry and Forensic Science, School of Natural Sciences, University of Kent, CT2 7NH Canterbury, UK. E-mail: m.k.chahal@kent.ac.uk*

and selective detection of acetone vapour under high humidity conditions.[26] Furthermore, analyte specificity can be controlled by varying the molecular structure of the porphyrin.[27] This extrinsic porous material is formed through multipoint supramolecular interactions including π–π stacking, metal coordination, and hydrogen bonding.

To build on this, we hypothesised that variation of metalation could influence supramolecular interactions and crystal packing due to conformational and coordinative changes at the porphyrin core, which might lead to gas uptake selectivities. Here, we report a series of metalloporphyrin compounds, Cu-OX1 (**1**), H2-OX1 (**2**), Ni-OX1 (**3**), Co-OX1 (**4**), Zn-OX1 (**5**) and Ni-OX3 (**6**), where the effect of the central metal atom (or its absence) on the porosity of the resulting processable porous materials (Fig. 1) and also the potential of these materials for selective CO_2/N_2 uptake, have been studied. Synthetic details are given in the SI. Co-OX1 (**4**) was synthesised by exchanging Ni(II) for Co(II) since the formylation route previously used for Ni-OX1 (**3**)[28] is incompatible with Co(II), leading to mixtures of oxidised products. Cu-OX1 (**1**) was synthesised following the formylation route, followed by reaction with 5,6-diaminopyrazine-2,3-dicarbonitrile, then oxidation using DDQ or PbO_2. The compounds were characterised using spectroscopic techniques (Fig. S1–S9) and single crystal X-ray diffraction studies.

Single crystals of Cu-OX1 (**1**), Ni-OX1 (**3**), Co-OX1 (**4**) and Ni-OX3 (**6**) were grown from suitable solvents. Ni-OX1 (**3**) (CCDC number: 1920462)[29] and Ni-OX3 (**6**) (CCDC numbers: 2107801–2107804)[26] were reported previously.[26] The complexes exhibit supramolecular structures formed through different non-covalent interactions (π–π stacking, hydrogen bonding, metal to ligand co-ordination); see Fig. S10–S27. For Cu-OX1 (**1**), there are four molecules per unit cell with π–π bonds (dimer shortest distance of 3.38(1) Å) and an H-bond, 3.49(8) Å between C═O and phenol H. $CHCl_3$ molecules are trapped inside the extended framework as shown in Fig. S11. Molecules of Ni-OX1 (**3**) form π–π dimers in the solid state with a short intermolecular closest approach of 3.28(4) Å and a C≡N···Ni(II) distance of 3.52(9) Å (Fig. S17). Co-OX1 (**4**) forms an extended network similar to Cu-OX1 (**1**) with a π-stacking distance of 3.30(9) Å and a longer H-bond distance of 3.55(6) Å between C═O and phenol H (Fig. S22). The magnitude of mean displacement of the 24-atom core (Δ24) and β-pyrrole carbons in Ni-OX1 (**3**) (Δ24 = 0.284 Å, ΔC_β = 0.365 Å) and Ni-OX3 (**6**) (Δ24 = 0.471 Å, ΔC_β = 0.330 Å) is much larger than in Cu-OX1 (**1**) (Δ24 = 0.070 Å, ΔC_β = 0.072 Å) or Co-OX1 (**4**) (Δ24 = 0.090 Å, ΔC_β = 0.135 Å) suggesting that both Cu-OX1 (**1**) and Co-OX1 (**4**) have quasi-planar conformations while the Ni-complexes in both OX1 and OX3 forms are nonplanar (Fig. S28).

The crystalline nature of the compounds was confirmed by powder X-ray diffraction (PXRD) studies (Fig. S29), and their permanent porosities were investigated by measuring N_2 sorption isotherms at 77 K (Fig. 2). To ensure removal of guest molecules, all samples were degassed under vacuum at 120 °C for 24 h prior to N_2 sorption measurements. Important textural parameters derived from these measurements are shown in Table S1, indicating that each system exhibits characteristic N_2 uptake, Brunauer–Emmett–Teller (BET) surface area and pore volume. Ni-OX1 (**3**) shows negligible N_2 uptake (15.33 $cm^3\ g^{-1}$) with a BET surface area of 15.12 $m^2\ g^{-1}$. Previously, we proposed that a highly non-planar porphyrin core (Δ24 displacement of the porphyrin mean planes) was required for effective N_2 adsorption.[26] However, surprisingly, the planar derivatives Cu-OX1 (**1**) and Co-OX1 (**4**) exhibit some of the largest BET surface areas and N_2 uptakes. This observation suggests that the porphyrin core structure is not the only factor influencing adsorption properties in these systems, but metalation and/or the identity of the coordinated metal atom also plays a significant role in influencing gas adsorption. The BET surface areas, N_2 uptakes and corresponding pore volumes for each system are summarised in Table 1.

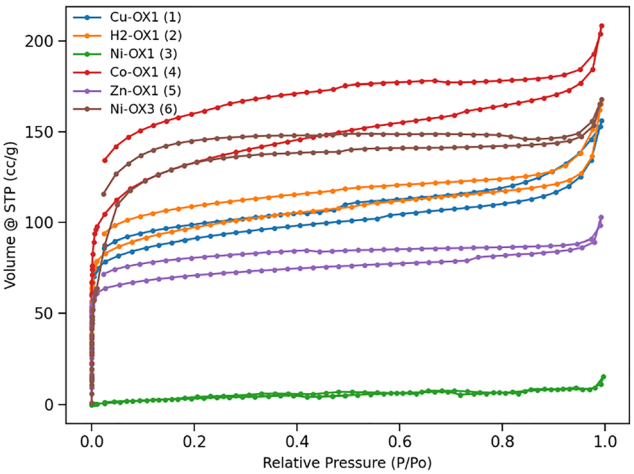

Fig. 2 N_2 adsorption–desorption isotherms at 77 K for M-OX1 and Ni-OX3 materials.

Given the different N_2 uptakes at 77 K under gas saturation conditions, we proceeded to investigate CO_2 uptake at 195 K and also under saturation conditions to assess the maximum CO_2 adsorption capacity of these complexes (Fig. 3). The CO_2 uptake capacities shown in Table 1 indicate that Ni-OX3 (**6**) has the lowest affinity towards CO_2. CO_2 and N_2 uptake data at 195 K and 77 K, respectively, reveal that Ni-OX1 (**3**) exhibits a substantially higher affinity for CO_2 (106.65 $cm^3\ g^{-1}$) than for N_2 (15.33 $cm^3\ g^{-1}$). This suggests an ultra-microporous structure since enhanced CO_2 uptake is most likely due to the smaller kinetic diameter of CO_2, which facilitates its diffusion into smaller pores. This observation is consistent with Ni-OX1 (**3**) having the lowest pore volume (0.040 $cm^3\ g^{-1}$) of the systems studied. All the materials studied show significant CO_2 uptakes

Table 1 BET surface areas (in $m^2\ g^{-1}$), N_2 uptakes and corresponding pore volumes ($cm^3\ g^{-1}$) at 77 K, and CO_2 uptakes (in $cm^3\ g^{-1}$) at 195 K for M-OX1 and Ni-OX3 complexes

Compound	BET surface areas	N_2 uptakes	Pore volumes	CO_2 uptakes
Cu-OX1 (**1**)	450.57	156.14	0.304	127.96
H2-OX1 (**2**)	450.71	165.28	0.296	133.94
Ni-OX1 (**3**)	15.12	15.33	0.040	106.65
Co-OX1 (**4**)	509.91	208.51	0.338	120.41
Zn-OX1 (**5**)	346.58	103.10	0.162	122.15
Ni-OX3 (**6**)	343.56	167.95	0.249	95.07

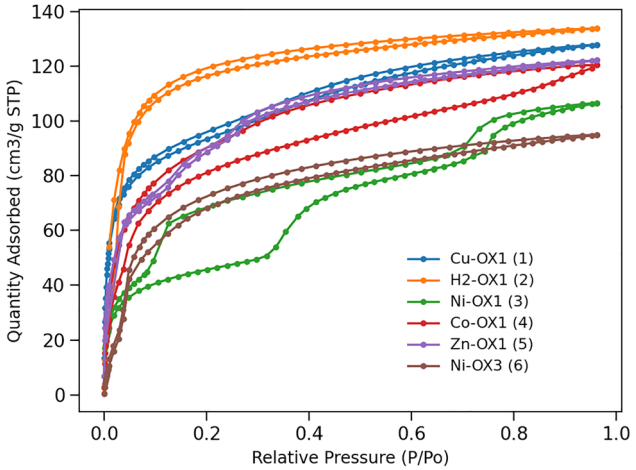

Fig. 3 CO_2 adsorption–desorption isotherms at 195 K for M-OX1 and Ni-OX3 materials.

making them suitable for applications involving efficient CO_2 adsorption, such as gas separation or carbon capture. Both Ni-OX1 (**3**) and Co-OX1 (**4**) exhibit hysteresis in their adsorption/desorption curves which can be attributed to phase transition occurring during the process. These phenomena are also confirmed by the PXRD patterns obtained before and after CO_2 adsorption as shown in Fig. S32 and S33 where the PXRD patterns differ especially in the low angle regions.

PXRD data obtained prior to and following CO_2 uptake studies indicate that the crystalline structure is retained after activation at 110 °C, although some phase transitions in the materials are observed (Fig. S30–35). Thermogravimetric analyses (Fig. S36) of the porous frameworks indicate weight losses starting at 50 °C complete by 170 °C assigned to solvent losses. The materials then exhibit a steady plateaux up to 380 °C, followed by weight losses of 45–59% occurring up to 900 °C assigned to decomposition. These data indicate that both the free-base and metal complexes have excellent thermal stability.

Considering the excellent thermal stability and selective gas uptake by Ni-OX1 (**3**), the suitability of these porphyrin complexes for gas separation applications was studied. While processable porous materials have been studied for gas separation, the impact of metalation and central atom identity at the porphyrin core remains unexplored, although it might be used to identify a wide range of useful materials without the need for *de novo* design. For this purpose, we conducted N_2 and CO_2 sorption experiments both at 273 K and 298 K (Fig. 4). All the materials studied show higher CO_2 uptakes at both 273 K and 298 K than their N_2 adsorption capacities as shown in Table 2. H2-OX1 (**2**) demonstrated the highest CO_2 uptake of 67.65 $cm^3\ g^{-1}$ at 273 K when compared to metal-containing compounds. However, at 298 K, the CO_2 uptake of the metal compounds exceeded that of H2-OX1 (**2**), with Co-OX1 (**4**) showing the highest uptake of 51.66 $cm^3\ g^{-1}$. These uptake values at 298 K are important for practical applications, as direct CO_2 capture from the atmosphere under ambient conditions is the key for industrial processes. These results highlight the role of metal ions in tuning the CO_2 uptake behaviour. Additionally, these CO_2 adsorption capacities are larger than

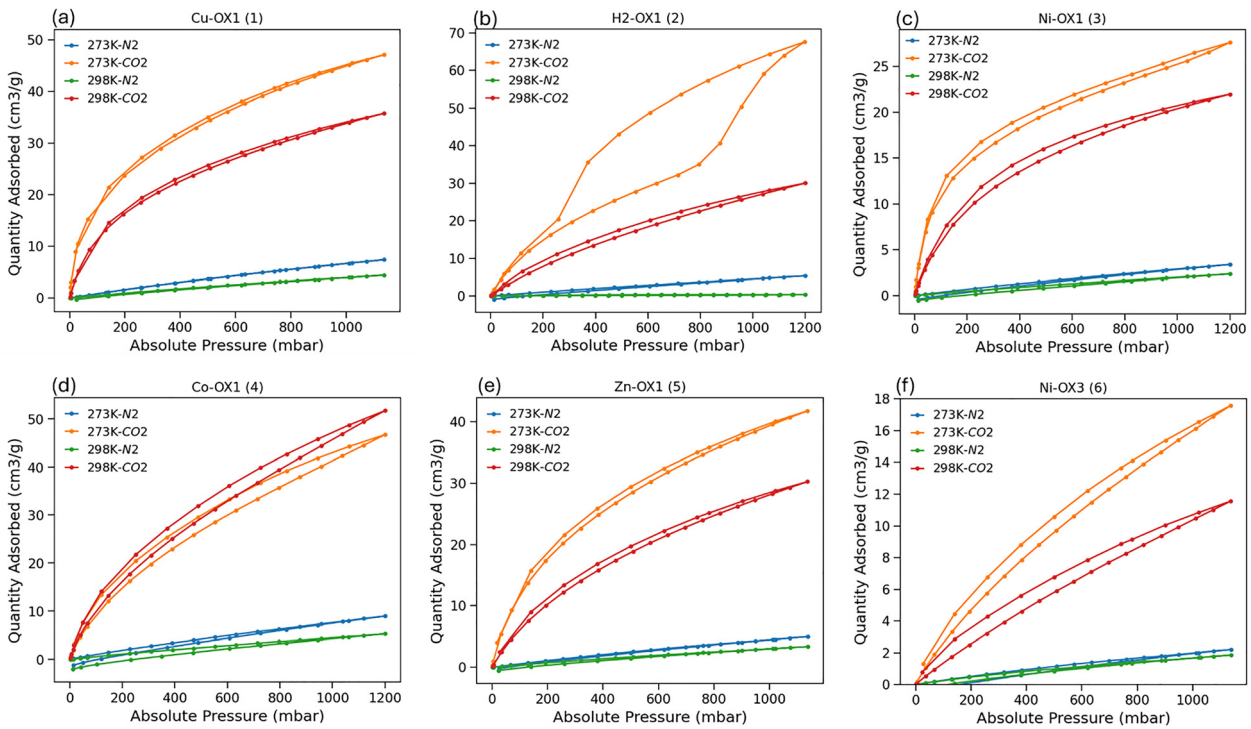

Fig. 4 CO_2 and N_2 adsorption isotherms at 273 K and 298 K, respectively for (a) Cu-OX1 (**1**); (b) H2-OX1 (**2**); (c) Ni-OX1 (**3**); (d) Co-OX1 (**4**); (e) Zn-OX1 (**5**); and (f) Ni-OX3. (**6**).

Table 2 CO_2 and N_2 adsorption capacities (in $cm^3\ g^{-1}$) at 273 K and 298 K for M-OX1 and Ni-OX3 complexes

Compound	CO_2 uptakes at 273 K	CO_2 uptakes at 298 K	N_2 uptakes at 273 K	N_2 uptakes at 298 K
Cu-OX1 (**1**)	47.06	35.76	7.39	4.41
H2-OX1 (**2**)	67.65	30.04	5.36	0.38
Ni-OX1 (**3**)	27.61	21.96	3.39	2.37
Co-OX1 (**4**)	46.67	51.66	8.95	5.27
Zn-OX1 (**5**)	41.79	30.28	4.99	3.37
Ni-OX3 (**6**)	17.59	11.57	2.21	1.86

those already reported for other processable porphyrinic porous organic molecular materials (see Table S2) making our materials a significant advance in terms of possible applications. In this study, CO_2 sorption measurements were performed on the same samples at three different temperatures (195 K, 273 K, and 298 K), which indicates that the samples exhibit porosity over multiple measurement cycles. The N_2 adsorption capacities of these materials are significantly lower, ranging from 0.38 to 8.95 $cm^3\ g^{-1}$, highlighting their selectivity of adsorption. Also, Ni-OX3 (**6**) exhibits the lowest CO_2 sorption. The significant differences in CO_2 and N_2 adsorption capacities suggest that these materials could be effective for CO_2/N_2 separation. CO_2/N_2 selectivity was determined using the ideal adsorbed solution theory (IAST),[30,31] a reliable method for predicting selectivity in binary gas separations (Fig. S37–S48). For a 0.15/0.85 CO_2/N_2 mixture, the highest selectivity of 143.4 was calculated for H2-OX1 (**2**) at 298 K and 0.1 bar, but metal complexes also demonstrate good selectivity. For example, Cu-OX1 (**1**) has a selectivity of 44.0 and Ni-OX1 (**3**) showed a value of 34.8 at 0.1 bar. At 273 K, the IAST selectivity differs: Cu-OX1 (**1**) shows the highest CO_2/N_2 selectivity of 77.8 at 0.1 bar, followed by Ni-OX1 (**3**) with a selectivity of 72.7. In contrast, H2-OX1 (**2**) has a significantly lower selectivity of 9.2 at 0.1 bar. These high selectivity values indicate that varying the central atom in porphyrinic systems can be used to tune the properties of materials for gas separation applications.

In conclusion, we report the modulation of the CO_2/N_2 gas adsorption capabilities of a family of supramolecular porous porphyrins by varying the coordinated metal cation. Under saturation conditions, Ni-OX1 (**3**) shows negligible N_2 uptake (15.33 $cm^3\ g^{-1}$) while Ni-OX3 (**6**) and other metal and free-base OX1 complexes show significant adsorption. OX1 systems show substantial CO_2 uptake (up to 133.94 $cm^3\ g^{-1}$ for H2-OX1) at 195 K. Further experiments at 278 K and 298 K, along with IAST calculations, confirm selective CO_2 adsorption and separation. These materials are solution processable, and their solubility in common organic solvents offers an additional advantage by enabling applications beyond bulk sorption experiments, such as thin-film fabrication and device integration.

SM, PG, RC, YM, and LKS: investigation; validation; writing – review and editing. AGS, JPH: supervision; validation; writing – review and editing; funding acquisition. MKC: conceptualization; funding acquisition; synthesis; writing – original draft, review and editing.

MKC thanks the Royal Society of Chemistry (R23-0850952021) and the Royal Society (RG\R1\251071) for funding. AGS thanks the Royal Society for a University Research Fellowship (URF\R1\201168). This work made use of shared equipment at the Materials Innovation Factory (MIF) created as part of the UK Research Partnership Innovation Fund (Research England) and co-funded by the Sir Henry Royce Institute.

Conflicts of interest

There are no conflicts to declare.

Data availability

The data supporting this article have been included in the supplementary information (SI). Supplementary information: experimental methods, crystallographic details, thermal analysis, PXRD patterns, and IAST plots for selectivity prediction. See DOI: https://doi.org/10.1039/d5cc06796k.

CCDC 2501550 and 2501551 contain the supplementary crystallographic data for this paper.[32a,b]

References

1 D. Wang, J. Penuelas, Y. Tao, I. Loladze, C. Cai, L. Song, J. Zhang, G. Zhang, Y. Wang, W. Zhou, Q. Li and C. Zhu, *Global Change Biol.*, 2025, **31**, e70299.
2 L. J. R. Nunes, *Environments*, 2023, **10**, 66.
3 L. Pan, K. M. Adams, H. E. Hernandez, X. Wang, C. Zheng, Y. Hattori and K. Kaneko, *J. Am. Chem. Soc.*, 2003, **125**, 3062–3067.
4 L. Wang and R. Yang, *J. Phys. Chem. C*, 2011, **115**, 21264–21272.
5 A. H. Farmahini, S. Krishnamurthy, D. Friedrich, S. Brandani and L. Sarkisov, *Chem. Rev.*, 2021, **121**, 10666–10741.
6 N. Stock and S. Biswas, *Chem. Rev.*, 2012, **112**, 933–969.
7 G. Zhang, B. Hua, A. Dey, M. Ghosh, B. A. Moosa and N. M. Khashab, *Acc. Chem. Res.*, 2021, **54**, 155–168.
8 A. G. Slater and A. I. Cooper, *Science*, 2015, **348**, aaa8075.
9 J. Tian, P. K. Thallapally and B. P. McGrail, *CrystEngComm*, 2012, **14**, 1909–1919.
10 P. Sun, H. Dong, S. Lv, Y. Yin, G. Gong, L. Wang, J. Wang and S. Chen, *J. Mater. Chem. A*, 2024, **12**, 1128–1134.
11 Z. J. Lin, S. A. R. Mahammed, T. F. Liu and R. Cao, *ACS Cent. Sci.*, 2022, **8**, 1589–1608.
12 M. Liu, M. A. Little, K. E. Jelfs, J. T. A. Jones, M. Schmidtmann, S. Y. Chong, T. Hasell and A. I. Cooper, *J. Am. Chem. Soc.*, 2014, **136**, 7583–7586.
13 S. Hong, Md. R. Rohman, J. Jia, Y. Kim, D. Moon, Y. Kim, Y. H. Ko, E. Lee and K. Kim, *Angew. Chem., Int. Ed.*, 2015, **127**, 13439–13442.
14 W. Yang, B. Li, H. Wang, O. Alduhaish, K. Alfooty, M. A. Zayed, P. Li, H. D. Arman and B. Chen, *Cryst. Growth Des.*, 2015, **15**, 2000–2004.
15 Y. N. Gong, D. C. Zhong and T. B. Lu, *Angew. Chem., Int. Ed.*, 2025, **64**, e202424452.
16 L. Ma, H. Arman, Y. Xie, W. Zhou and B. Chen, *Cryst. Growth Des.*, 2022, **22**, 3808–3814.
17 J. H. Lee, H. Park, Y. Kim, D. Yim, T. Kim, J. Choi, Y. Lee and W. D. Jang, *ACS Appl. Mater. Interfaces*, 2023, **15**, 57507–57513.
18 W. Yang, F. Yang, T. L. Hu, S. C. King, H. Wang, H. Wu, W. Zhou, J. R. Li, H. D. Arman and B. Chen, *Cryst. Growth Des.*, 2016, **16**, 5831–5835.
19 A. G. Slater, P. S. Reiss, A. Pulido, M. A. Little, D. L. Holden, L. Chen, S. Y. Chong, B. M. Alston, R. Clowes, M. Haranczyk, M. E. Briggs, T. Hasell, G. M. Day and A. I. Cooper, *ACS Cent. Sci.*, 2017, **3**, 734–742.
20 M. O'Shaughnessy, P. R. Spackman, M. A. Little, L. Catalano, A. James, G. M. Day and A. I. Cooper, *Chem. Commun.*, 2022, **58**, 13254–13257.
21 X. T. He, Y. H. Luo, Z. Y. Zheng, C. Wang, J. Y. Wang, D. L. Hong, L. H. Zhai, L. H. Guo and B. W. Sun, *ACS Appl. Nano Mater.*, 2019, **2**, 7719–7727.
22 Y. Cai, J. Gao, J. H. Li, P. Liu, Y. Zheng, W. Zhou, H. Wu, L. Li, R. B. Lin and B. Chen, *Angew. Chem., Int. Ed.*, 2023, **62**, e202308579.

23 P. Tholen, C. A. Peeples, M. M. Ayhan, L. Wagner, H. Thomas, P. Imbrasas, Y. Zorlu, C. Baretzky, S. Reineke, G. Hanna and G. Yücesan, *Small*, 2022, **18**, 2204578.
24 Q. Yin, E. V. Alexandrov, D. H. Si, Q. Q. Huang, Z. Bin Fang, Y. Zhang, A. A. Zhang, W. K. Qin, Y. L. Li, T. F. Liu and D. M. Proserpio, *Angew. Chem., Int. Ed.*, 2022, **61**, e202115854.
25 S. Huang, Y. Chang, Z. Li, J. Cao, Y. Song, J. Gao, L. Sun and J. Hou, *Adv. Funct. Mater.*, 2023, **33**, 2211631.
26 M. K. Chahal, S. Maji, A. Liyanage, Y. Matsushita, P. Tozman, D. T. Payne, W. Jevasuwan, N. Fukata, P. A. Karr, J. Labuta, L. K. Shrestha, S. Ishihara, K. Ariga, F. D'Souza, G. Yoshikawa, Y. Yamauchi and J. P. Hill, *Mater. Chem. Front.*, 2023, **7**, 325–332.
27 S. Maji, J. Hynek, K. Nakada, A. Hori, K. Minami, J. Labuta, M. K. Chahal, D. T. Payne, G. J. Richards, L. K. Shrestha, K. Ariga, Y. Yamauchi, G. Yoshikawa and J. P. Hill, *Adv. Mater. Technol.*, 2025, **10**, e00294.
28 M. K. Chahal and M. Sankar, *Dalton Trans.*, 2016, **45**, 16404–16412.
29 M. K. Chahal, J. Labuta, V. Březina, P. A. Karr, Y. Matsushita, W. A. Webre, D. T. Payne, K. Ariga, F. D'Souza and J. P. Hill, *Dalton Trans.*, 2019, **48**, 15583–15596.
30 C. M. Simon, B. Smit and M. Haranczyk, *Comput. Phys. Commun.*, 2016, **200**, 364–380.
31 Mantid, *Manipulation and Analysis Toolkit for Instrument Data*, 2013, Mantid Project, DOI: 10.5286/SOFTWARE/MANTID6.14.
32 (*a*) CCDC 2501550: Experimental Crystal Structure Determination, 2026, DOI: 10.5517/ccdc.csd.cc2pz25y; (*b*) CCDC 2501551: Experimental Crystal Structure Determination, 2026, DOI: 10.5517/ccdc.csd.cc2pz26z.